Characterizing white matter multi-fiber structure using the Riemann-Finsler framework in HARDI

Avinash Bansal[a], Sumit Kaushik[c,d,*], Temesgen Bihonegn[a], Denis Baručić[b], Peter T. While[c,d] and Jan Slovák[a]

[a]*Department of Mathematics, Faculty of Science, Brno, Czech Republic*

[b]*Department of Cybernetics, Czech Technical University in Prague, Prague, Czech Republic*

[c]*Department of Radiology and Nuclear Medicine, St. Olav's University Hospital, Trondheim, Norway*

[d]*Department of Circulation and Medical Imaging, NTNU - Norwegian University of Science and Technology, Trondheim, Norway*

ARTICLE INFO

ABSTRACT

The 2nd-order tensors obtained in diffusion tensor imaging (DTI) lie in a Riemann space. Scalars derived from DTI are helpful in the diagnosis of diseases related to white matter structures. However, the underlying limitation of the DTI model restricts the effective use of scalars in heterogeneous tissue structures. These can be modelled using higher-order tensors (HOTs) in high angular resolution diffusion imaging (HARDI). We introduce two descriptors that are helpful in classifying the voxels on the basis of the number of the underlying fibers with distinct orientation, which, in turn, relates to the anisotropy of water diffusion in biological tissues. These are computed based on the Riemann and Finsler geometry paradigms. The descriptor based on Finsler geometry is named Finsler fractional anisotropy (FFA). It can be applied to the orientation distribution function (ODF) computed from any HARDI model. The other descriptor, called FA4, is based on the Riemann framework. We compare their performance with those of the known Kelvin invariants in both synthetic and in vivo data.

1. Introduction

Diffusion magnetic resonance imaging (dMRI) has facilitated the study of microstructures in the human brain non-invasively. Diffusion tensor imaging (DTI), introduced by Basser et al. [1, 2], is well established in both clinical imaging and research. The framework for processing the positive definite 2nd-order tensors originates from the established theory of Riemann geometry [3, 4, 5, 6, 7]. Some of the prevalent anisotropy descriptors from 2nd-order tensors are mean diffusivity (MD), fractional anisotropy (FA), radial diffusivity (RD), and Hilbert anisotropy (HA). These can be considered as descriptors for analyzing the structure of tissues. Many clinical studies [8, 9, 10, 11, 12, 13] have indicated that changes in these quantities can detect changes in the diffusion of water molecules in unhealthy tissue. They demonstrated the clinical importance of those scalars in the examination of various diseases such as multiple sclerosis, Parkinson's disease, Alzheimer's dementia, etc.

DTI uses a Gaussian description of diffusion and, therefore, cannot describe regions of fiber crossing or merging. To model these heterogeneous tissue structures, increasing the number of measured diffusion gradient directions is helpful [14], and the acquisition protocol is known as high angular resolution diffusion imaging (HARDI). Any orientation distribution function (ODF) can be represented by higher-order tensors (HOTs) [15, 16]. There is a potential for anisotropy scalar measures from HOTs to be utilized in clinical studies as biomarkers [17, 18, 19, 20]. Generalized anisotropy (GA) [18] is evaluated using the variance of normalized diffusivities and involves arbitrary values to be chosen according to the data set for better contrast. Similar to FA, generalized fractional anisotropy (GFA) [19] evaluates the orientation distribution function ψ (ODF) peaks in multiple directions. Multi-directional anisotropy (MDA) [20] is closely related to GFA, but only takes into account ψ_{max} and ψ_{min}. However, a study on an atlas of 630 subjects showed that MDA and GFA vary in a similar manner to FA with respect to diffusion directions [21], and hence these scalars are also not sufficient for delineating regions of crossing fibers.

The Kelvin rotation-invariant descriptors from the 4th-order tensors proposed in [22] showed better performance than GFA. Their notation is based on the Voigt-Mandel 6×6 matrix form. The six basic invariants (S) and the six principal invariants (J) can be computed from the eigenvalues of the matrix form. Two of them are equal ($S41 = J41$), keeping the total number to eleven.

If a medium is both inhomogeneous and anisotropic, a Finsler metric is appropriate for defining the directional structure, since it is a function of both position and direction. Therefore, it is better suited to the description of multiple fibers than a Riemann metric. The Finsler metric has previously been used to assist tractography algorithms when applied to HARDI data in regions of crossing fibers [23, 24, 25]. Local Finsler diffusion tensors are approximations of higher-order tensors representing the complex geometry of fibers. This idea is the motivation for the present work.

In this work, we propose a descriptor, called Finsler fractional anisotropy (FFA) to characterize the underlying geometry of the fibers in a given voxel. The principal idea behind this work is the suitability of the Finsler framework for HARDI. This is due to the emergence of multiple metrics

per voxel, which allow us to characterize multiple fibers per voxel. One advantage of this method is that it can be applied to an ODF from any HARDI dataset.

In addition, we assess the performance of another descriptor, denoted as FA4, obtained from the Voigt-Mandel notation of the 4th-order diffusion tensor. This formulation is similar to FA in DTI (3D) but in 6D, $S^+(6)$.

We show that the proposed descriptors can characterize up to three fibers per voxel. We assess their performance in both synthetic and in vivo data. We summarize that along with Kelvin invariants, the proposed scalars also yield potentially useful information about fiber composition from diffusion data.

This paper is organized as follows: Section 2 contains a concise introduction to diffusion modelling and the formulation of the Finsler metric for a higher-order tensor. Section 3 presents the method to obtain a descriptor from the Finsler metrics and another one from the 6×6 matrix Voigt-Mandel representation of the 4th-order diffusion tensor. It should be noted that these descriptors are formulated from different approaches. Section 4 describes experiments and results, where we compare the performance of the descriptors. The last section 5 is dedicated to the conclusion and further comments.

2. Theory

The magnetic resonance (MR) signal attenuation associated with the diffusion of water molecules in tissue can be modelled using the generalized Stejskal-Tanner equation,

$$S(\mathbf{v}) = S_0 \exp(-bD(\mathbf{v})), \tag{1}$$

with the diffusion weighting coefficient b, and

$$D(\mathbf{v}) = \sum_{i=1}^{3} \sum_{j=1}^{3} \cdots \sum_{k=1}^{3} \sum_{l=1}^{3} D_{ij\ldots kl} \mathbf{v}_i \mathbf{v}_j \cdots \mathbf{v}_k \mathbf{v}_l, \tag{2}$$

where $D_{ij\ldots kl}$ are the diffusion coefficients (tensor) and $\mathbf{v}_i$ is the i-th component of the magnetic gradient vector $\mathbf{v}$, $|\mathbf{v}| = 1$. Tuch et al. [14] demonstrate how revealing gradient directions can provide insight into the detailed shape of biological tissues in their work.

Due to antipodal symmetry, the tensors are of even order, and since the diffusion process is a physical phenomenon, HOTs are ensured to have a positive definite property [26, 27]. By the assumed complete symmetry, the number of independent coefficients for an nth-order tensor is reduced from 3^n to $\frac{1}{2}(n+1)(n+2)$. For instance, for a 4th-order tensor, there are 15 independent coefficients out of the total $3^4 = 81$.

2.1. Related work

Riemannian geometry is used for the description of inhomogeneous and isotropic media. For non-isotropic and inhomogeneous media, the Finsler geometry is more suitable [23]. For diffusion MRI, this framework is used to model the geometry of brain tissue as Finsler manifolds by

deriving Finsler functions from the diffusion-weighted signals. There is a correlation between the large-scale structural orientation of white matter and the local amount of diffusion found in a specific direction [28].

For 2nd-order tensors, many scalars have been introduced in the literature. A number of authors have addressed the computational framework and its application in the context of DTI [22, 29, 30]. Extending DTI to HARDI to deal with multi-fiber configurations, previous works [18, 19, 20, 22] have proposed GA, GFA, MDA, and Kelvin scalars, respectively. Kelvin invariants provide multiple contrast maps that capture diffusion information.

2.2. Finsler metric

The Finsler metric is computed from the Hessian of the Finsler norm. The Finsler norm for a 4th-order tensor, as proposed in [24], satisfies differentiability, homogeneity, and strong convexity properties. We use the Einstein summation notation[1] to represent a 4th-order symmetric tensor that can be fitted to the ODF data. A Finsler norm $F(\mathbf{x}, \mathbf{y})$ corresponding to a 4th-order tensor can be defined as

$$F(\mathbf{x}, \mathbf{y}) = (D_4(\mathbf{x}, \mathbf{y}))^{1/4}, \tag{3}$$

with

$$D_4(\mathbf{x}, \mathbf{y}) = D_{ijkl}(\mathbf{x}) y^i y^j y^k y^l, \tag{4}$$

where $\mathbf{x}$ is the position, $\mathbf{y}$ is the direction, and D_4 is the fully symmetric tensor of 4th-order. The Finsler metric g_{ij} for each choice of $\mathbf{y}$ is defined as

$$g_{ij}(\mathbf{x}, \mathbf{y}) = \frac{1}{2} \frac{\partial^2 F^2(\mathbf{x}, \mathbf{y})}{\partial y^i \partial y^j}. \tag{5}$$

The convex property ensures that the 2nd-order metric tensors (with size 3×3) are strictly positive definite. These metric tensors are related to the distribution of fiber orientations.

3. Proposed methods

The proposed descriptors require evaluation of a 4th-order tensor at each voxel. We use the method introduced in [26] to ensure the positive definiteness of the tensor D_4, in equation (4), with coefficients D_{ijkl}, where $i, j, k, l \in \{1, 2, 3\}$.

3.1. Finsler fractional anisotropy (FFA)

We determine the Finsler scalar from HARDI data. Unit gradient vectors $\mathbf{v}_s$ are fed to the Finsler norm, which produces a local 2nd-order diffusion tensor $g_{ij}(\mathbf{x}, \mathbf{v}_s)$ corresponding to $\mathbf{v}_s$ (by equation (5)).

By definition, a Finsler metric is both position and direction dependent; therefore, a set of these metrics encodes multiple fiber directions within each voxel. To quantify this information, we propose the scalar FFA to be equal to the

---

[1]Einstein notation: whenever two indices with the same labels appear on the same side of an equation, one assumes that there is an implicit sum over those indices.

regular fractional anisotropy of the mean of these Finsler metrics (quadratic forms) at position **x**, expressed as

$$\text{FFA}(\mathbf{x}) = \text{FA}\left(\frac{1}{p} \sum_{s=1}^{p} g_{ij}(\mathbf{x}, \mathbf{v}_s) \right), \tag{6}$$

where p is the number of gradient directions that lie on the hemisphere. The sum of positive definite quadratic forms is also positive definite. Since FFA(**x**) is defined as a fractional anisotropy (FA), it lies in [0, 1]. Note that the FFA can be computed for any set of gradient directions, and so it can also be used to explore the diffusion profile in any specific direction.

3.2. Anisotropy measure from 4th-order tensor (FA4)

A 3D 4th-order tensor can be represented in Voigt-Mandel 6×6 matrix form, which has been shown to be preferable to alternative representations [31, 32]. This 6D 2nd-order tensor lies in a Riemann space $S^+(6)$, which does not distinguish between contravariant and covariant components. Nevertheless, its form permits convenient tensor operations. For example, the inverse components of the original 3D 4th-order tensor can be found simply by inverting the Voigt-Mandel matrix. Kelvin invariants can be derived from the eigenvalues $\lambda_1, \dots, \lambda_6$ of the Voigt-Mandel 6×6 matrix form. The set of basic invariants are

$$\begin{aligned}
S41 &= \lambda_1 + \lambda_2 + \lambda_3 + \lambda_4 + \lambda_5 + \lambda_6, \\
S42 &= \lambda_1^2 + \lambda_2^2 + \lambda_3^2 + \lambda_4^2 + \lambda_5^2 + \lambda_6^2, \\
S43 &= \lambda_1^3 + \lambda_2^3 + \lambda_3^3 + \lambda_4^3 + \lambda_5^3 + \lambda_6^3, \\
S44 &= \lambda_1^4 + \lambda_2^4 + \lambda_3^4 + \lambda_4^4 + \lambda_5^4 + \lambda_6^4, \\
S45 &= \lambda_1^5 + \lambda_2^5 + \lambda_3^5 + \lambda_4^5 + \lambda_5^5 + \lambda_6^5, \\
S46 &= \lambda_1^6 + \lambda_2^6 + \lambda_3^6 + \lambda_4^6 + \lambda_5^6 + \lambda_6^6,
\end{aligned} \tag{7}$$

and the principal invariants are

$$\begin{aligned}
J41 &= S41, \\
J42 &= \sum_{i<j} \lambda_i \lambda_j, \\
J43 &= \sum_{i<j<k} \lambda_i \lambda_j \lambda_k, \\
J44 &= \sum_{i<j<k<l} \lambda_i \lambda_j \lambda_k \lambda_l, \\
J45 &= \sum_{i<j<k<l<m} \lambda_i \lambda_j \lambda_k \lambda_l \lambda_m, \\
J46 &= \lambda_1 \lambda_2 \lambda_3 \lambda_4 \lambda_5 \lambda_6,
\end{aligned} \tag{8}$$

where $i, j, k, l, m = 1, \dots, 6$.

The eigenvalues obtained from the Voigt-Mandel representation for a tensor of 4th-order provide information about the diffusivity profile along principle axes. Therefore, inspired by the expression for generalized fractional anisotropy [19], we propose another scalar FA4 as a function of these eigenvalues, which is a possible alternative to the Kelvin invariants. In the 6D hyper-ellipsoid case, FA4 is defined as

$$\text{FA4} = \sqrt{\frac{6}{5} \frac{\sum_i (\lambda_i - \lambda_a)^2}{\sum_i \lambda_i^2}}, \tag{9}$$

and lies in (0, 1], where $\lambda_a = \frac{1}{6} \sum_{i=1}^{6} \lambda_i$ represents the average diffusion in a voxel.

4. Experiments and results

We used the Matlab fanDTasia ToolBox [26, 27] to produce synthetic images that closely mimic the diffusion of water in white matter fibers. We used $b = 1500 s/mm^2$ and 81 different gradient directions. We also had access to in vivo data using 64 gradient directions from a healthy volunteer with consent.

The in silico experiments were carried out on a desktop with an Intel(R) Core(TM) i5-7500T CPU @ 2.70GHz and 16GB RAM using MATLAB 2019a.

In the first experiment, we simulated four groups of tensors representing: isotropic diffusion, one fiber, two fibers, and three fibers. In the latter two cases, the crossing angle was kept at 90°. Multiple instances of each group (tensors) were generated by rotating the individual fiber directions 50 times and maintaining the same crossing angle.

Box-and-whisker plots for FFA and FA4 are shown in Fig. 1 when calculated on the synthetic data under several different levels of Rician noise. Both descriptors are able to separate the interquartile ranges (IQRs) of the four groups without noise, and at a low noise level (0.01). We observe that at higher levels of noise (0.09), the descriptors possibly confound the case of three fibers with the case of isotropic diffusion.

Table 1 shows the mean and standard deviations of the two proposed descriptors under rotations. The low standard deviations reflect their invariance to rotations.

Table 2 shows the results of t-tests on the generated synthetic data. Low p-values ($p \ll 0.01$) in nearly every t-test (i.e., Rician noise level ≤ 0.05) indicate strong evidence of significant differences between the four groups for both metrics.

Fig. 2 demonstrates the sensitivity of the proposed scalars with respect to the angle between the underlying fibers. The graph indicates that FFA can discern a wider range of angle differences (i.e., going from one fiber to two orthogonal fibers).

For comparison with the Kelvin invariants, Fig. 3 shows the results for a selection of S and J scalars (out of 12) that possess distinct characteristics. Two of these scalars, S41 and J44 (first and last rows, respectively), fail to characterize the fibers. S43 and J42 perform similarly to FFA and FA4, but either they provide inverted contrast (J42), which is non-intuitive, or their range is unbounded, which limits their practical use.

Fig. 4 (a) shows a simulated tensor field with diverse crossing configurations obtained by combinations of linear

Table 1
The mean and standard deviation of FFA and FA4 under 50 different fiber rotations for the four cases of different numbers of orthogonal fibers.

Number of fibers	FFA	FA4
Isotropic	0.00 ± 0.000	0.45 ± 0.000
One	0.89 ± 0.003	0.99 ± 0.000
Two	0.59 ± 0.002	0.88 ± 0.002
Three	0.06 ± 0.008	0.77 ± 0.002

Table 2
The p-values obtained for the six possible pairs of features using the t-test. The low values indicate significant statistical differences between the means of the two distributions. Here "}" represents $p \ll 0.01$.

p-values from t-test				
Rician Noise:	≤ 0.05		0.09	
Possible pairs	FFA	FA4	FFA	FA4
Isotropic vs. one				
Isotropic vs. two				
Isotropic vs. three	}	}	0.71	}
One vs. two				
One vs. three				
Two vs three				

and curved fibers, forming four regions. The corresponding grayscale images of the descriptors FFA and FA4 are shown in the same row. The remaining rows show the images of the Kelvin invariants. The proposed descriptors are capable of discriminating the different regions. In contrast, most of the Kelvin invariants provide poor contrast between regions, with the exception of S42 and J42.

Fig. 5 demonstrates that subsets of gradient directions can be used in calculating FFA to probe specific structural directionality.

Fig. 6 shows the performance of the proposed descriptors and Kelvin invariants on the in vivo data of the brain (axial slice). Some Kelvin invariants, such as J44, J45, and J46, completely fail to retain any structural information, and others provide limited contrast information. FFA and FA4, on the other hand, provide clear and detailed contrast throughout the brain, clearly delineating, for example, the white and grey matter regions.

Fig. 7 illustrates the FFA maps for the in vivo data computed using different directions. The different maps show sensitivity to the directionality of the underlying water diffusion in the tissue. Note that it is possible to obtain a large set of these maps considering many gradient directions.

For the classification of different tissue types, appropriate ranges of descriptor values should ideally be chosen by assessing the results obtained for in vivo data combined with knowledge of brain anatomy. Here, however, we propose one possible set of classification ranges in Table 3, as guided by the results for the synthetic data displayed in Fig. 1.

Table 3
The chosen ranges of scalar values used for classifying the voxels in an in vivo image in terms of the expected number of fibers with distinct orientation.

Number of fibers	Ranges	
	FFA	FA4
One	$[0.70, 1.00]$	$(0.92, 1.00]$
Two	$[0.40, 0.70)$	$(0.80, 0.92)$
Three	$[0.2, 0.40)$	$(0.65, 0.80)$
Isotropic	$[0.00, 0.2)$	$[0.40, 0.65)$

Fig. 8 illustrates the corresponding classification of voxels for the in vivo data. The voxels are coloured as follows: red for one fiber, green for two fibers, blue for three fibers, and black for the isotropic regions. The proposed descriptors show similar performance.

5. Conclusion and further comments

In an earlier work [22], Kelvin invariants were shown to provide a richer set of contrast maps than other existing scalars. Here we have introduced the FFA descriptor based on nonlinear Finsler geometry. This is formulated from the multiple Finsler metrics obtained at each voxel. Individually, these metrics hold local diffusion information. Therefore, we can obtain multiple scalar maps using these metrics. In this work, we proposed FFA in terms of a simple averaging of the Finsler metrics. However, other descriptors based on alternative functions of these Finsler metrics have the potential to provide other useful contrast, and this will be explored in further work. We also proposed another descriptor, FA4, which, similar to the Kelvin invariants, is expressed as a function of the eigenvalues of the Voigt-Mandel matrix, yet with the possible advantage that it is bounded between zero and unity.

We have compared the performance of FFA and FA4 with the Kelvin invariants, using both synthetic and in vivo data. Their performance was discussed by considering statistical significance tests and by assessing the maps acquired using both synthetic and in vivo data. Our proposed descriptors were shown to provide more relevant contrast in terms of anisotropy than most of the Kelvin invariants, and do not require careful windowing of intensities for visualizing the maps. As an advantage, the FFA descriptor can be obtained from an ODF corresponding to any HARDI model, in comparison to FA4 which is only applicable to 4th-order tensors. Furthermore, FFA uses a broader range of values to characterize multi-fiber regions. In conclusion, these novel descriptors have the potential to be used as biomarkers. A set of experiments are sought as the next step to assess the efficacy of these descriptors in a clinical setting.

Compliance with Ethical Standards
This is a numerical study for which no ethical approval was required.

Acknowledgments
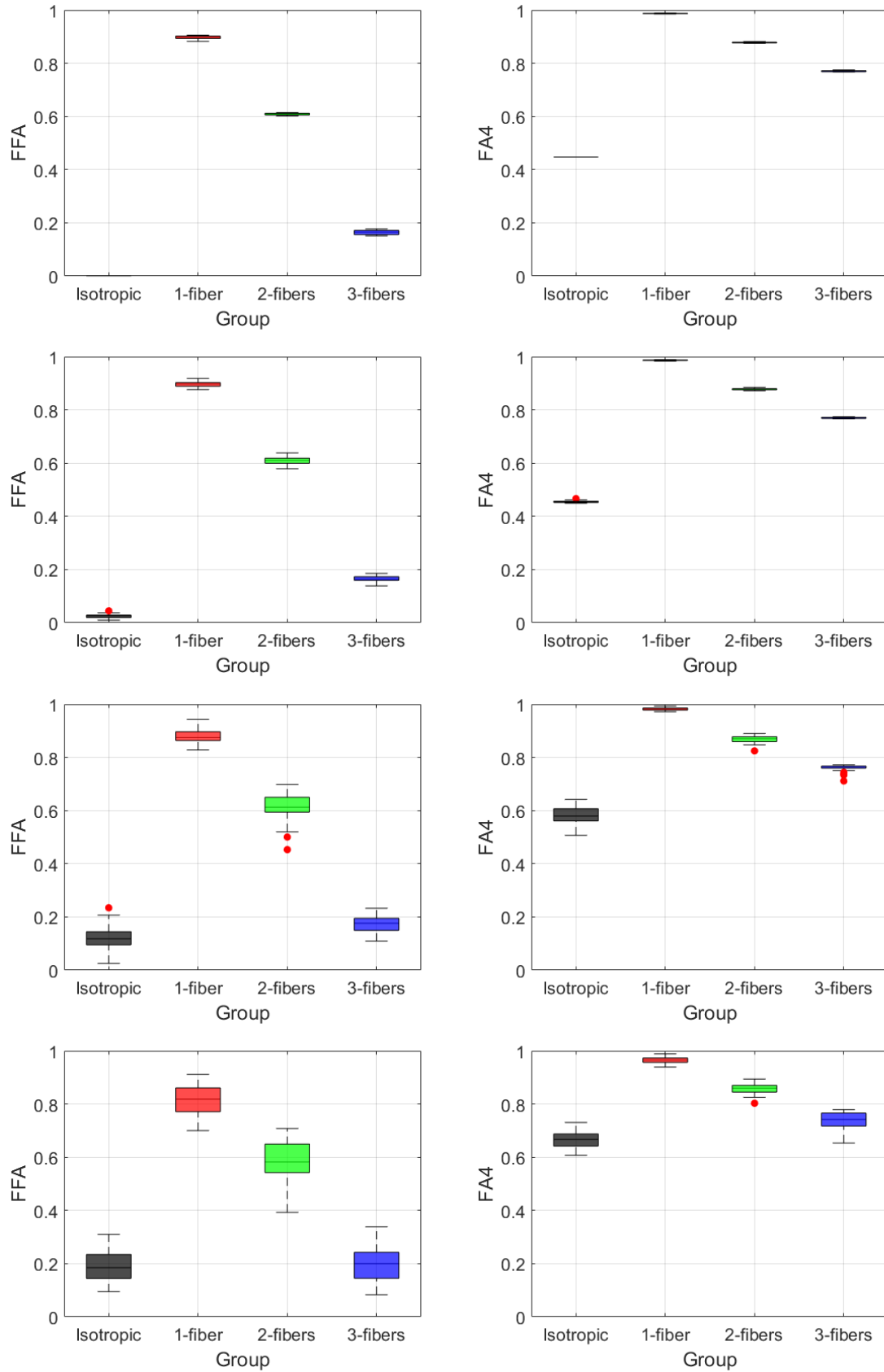
Figure 1: Box-and-whisker plots of FFA (left) and FA4 (right) for the four groups of synthetic data representing different numbers of orthogonal fibers (colours). Each row shows results for different levels of Rician noise (top-bottom): without noise, 0.01, 0.05, and 0.09.
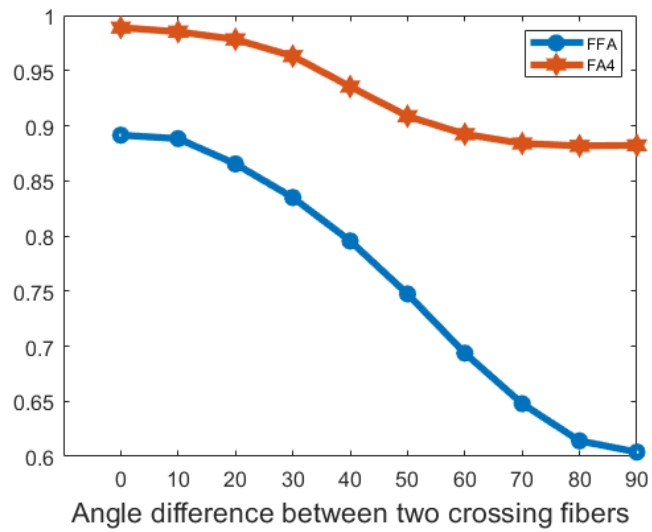
Figure 2: Line plots of FFA and FA4 with respect to the angle between two crossing fibers (synthetic data without noise).
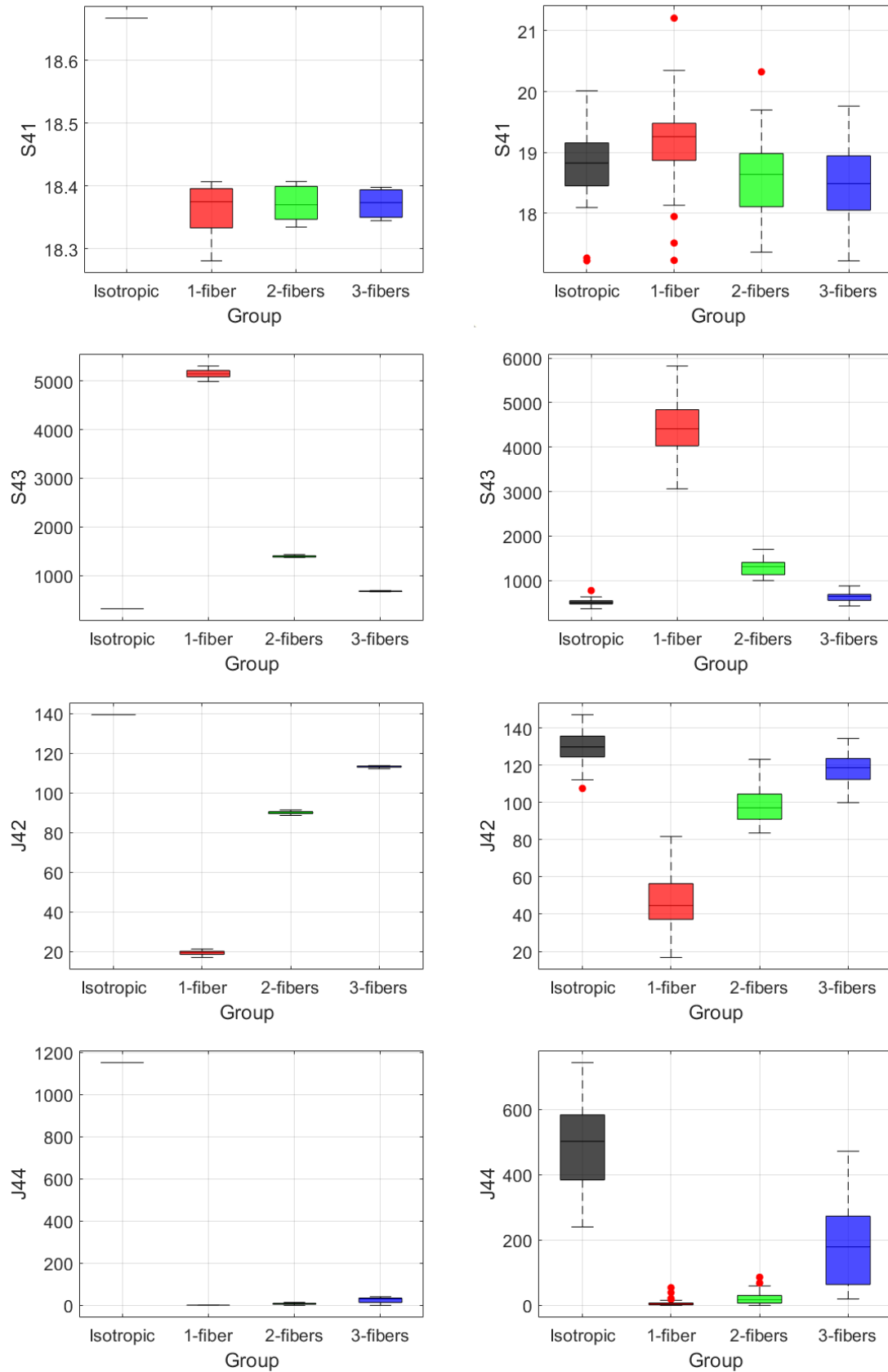
Figure 3: Box-and-whisker plots of a selection of Kelvin invariants (top-bottom: S41, S43, J42, J44) for the four groups of synthetic data representing different numbers of orthogonal fibers (colours). Each column shows results for different levels of Rician noise: (left) without noise; (right) 0.09.

(a) 4th-order tensor image

(b) FFA

(c) FA4

(d) S41

(e) S42

(f) S43

(g) S44

(h) S45

(i) S46

(j) J42

(k) J43

(l) J44

(m) J45

(n) J46
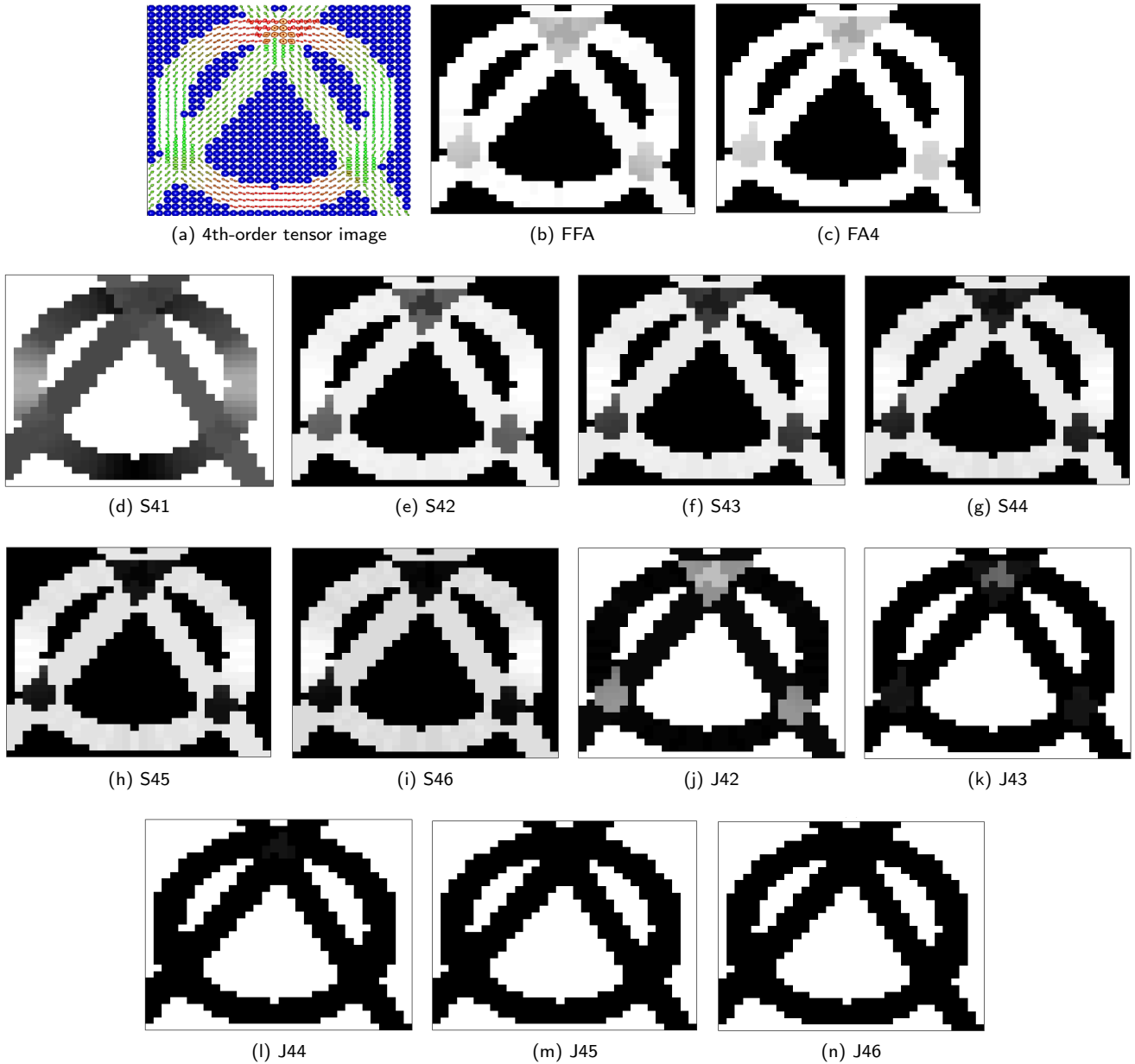
Figure 4: (a) Synthetic tensor field image (created by intersecting two linear fibers and a curved fiber, forming four distinct groups comprising isotropic diffusion, one fiber, two fibers, and three fibers), and corresponding maps of (b) FFA, and (c) FA4. The remaining rows show corresponding maps of the Kelvin invariants.

(a) 4th-order tensor image

(b) FFA x-axis

(c) FFA y-axis
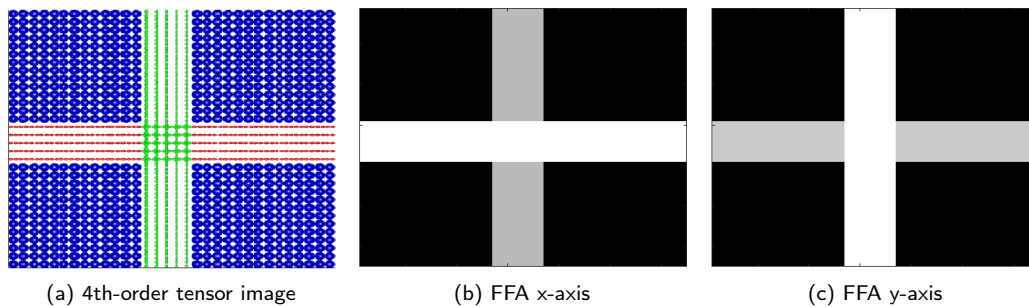
Figure 5: (a) Synthetic tensor field image, (b) and (c) FFA scalar maps considering only the x and y directions, respectively.

(a) Brain tensor field (axial view) (b) FFA (c) FA4

(d) S41 (e) S42 (f) S43

(g) S44 (h) S45 (i) S46

(j) J42 (k) J43 (l) J44

(m) J45 (n) J46
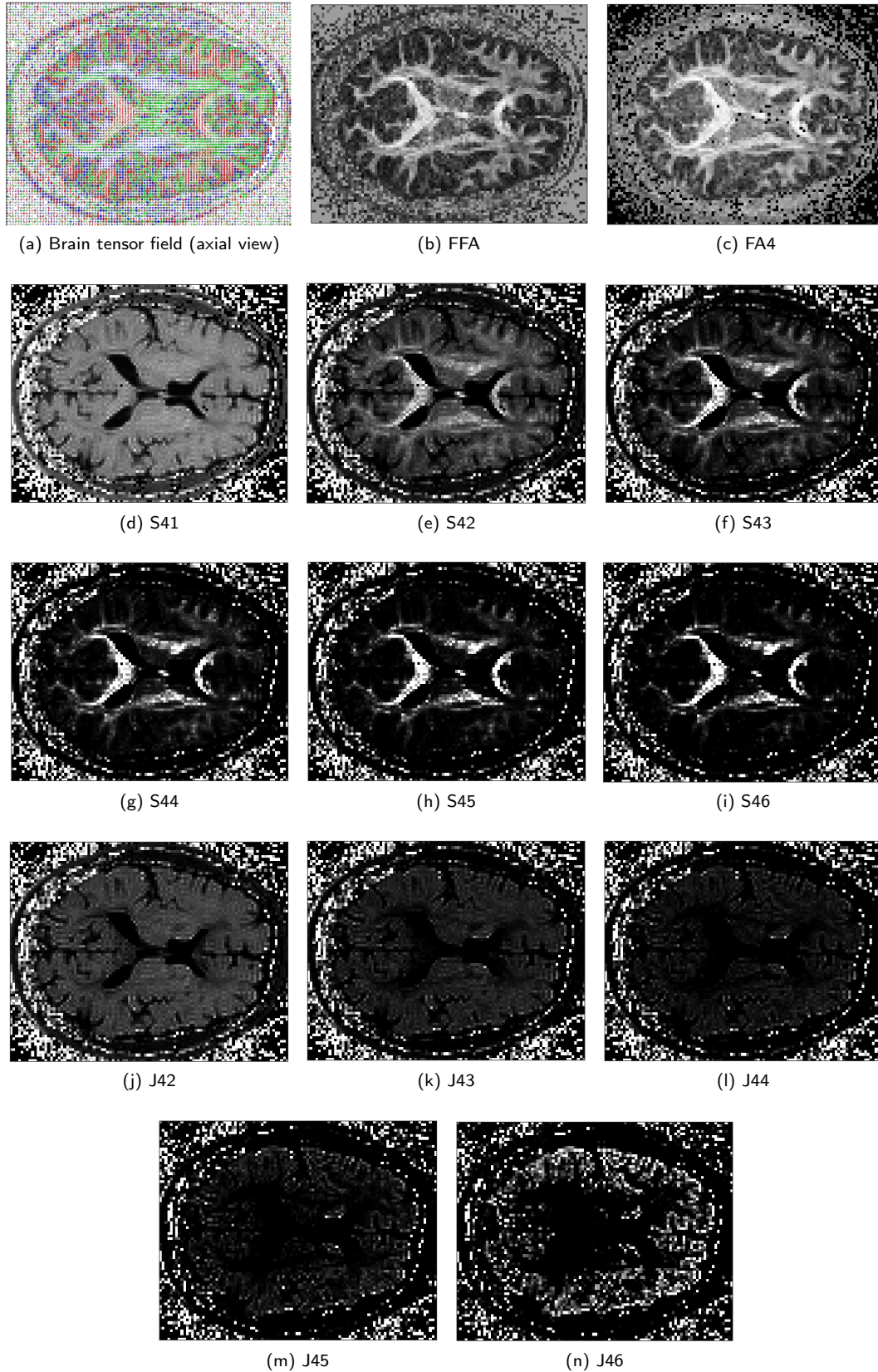
Figure 6: (a) 4th-order tensor field image for the in vivo data (brain, axial slice), and corresponding maps of (b) FFA, and (c) FA4. The remaining rows show corresponding maps of the Kelvin invariants. The Kelvin invariant maps are displayed by windowing the intensity values such that the minima and maxima equal the 10th and 90th percentiles, respectively.

(a) FFA x-axis   (b) FFA y-axis   (c) FFA z-axis
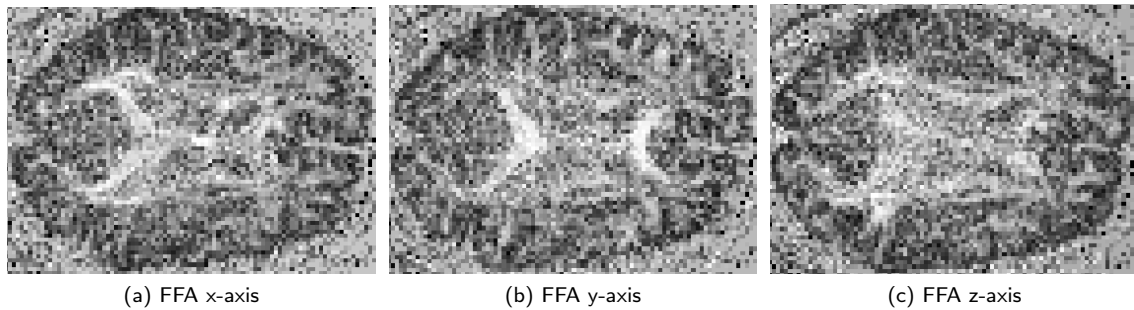
Figure 7: Maps of FFA for the in vivo data (brain, axial slice) considering different orientations separately. These maps show different contrasts that capture the respective directionality of the diffusion in different regions. Such maps can be obtained for any chosen gradient direction.

(a) FFA   (b) FA4
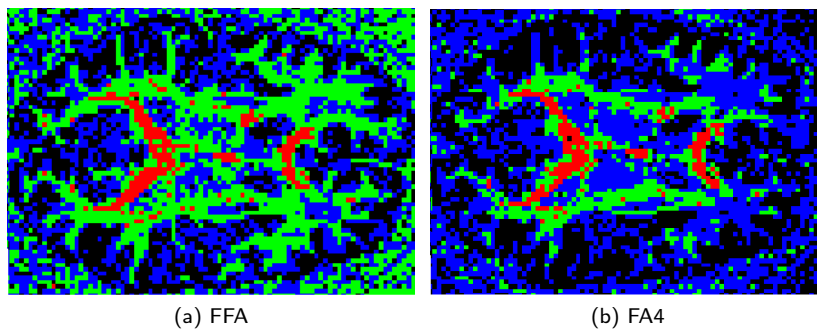
Figure 8: Maps showing the classification of voxels for the in vivo data (brain, axial slice) based on the descriptors using the ranges given in Table 3 (red for one fiber, green for two fibers, blue for three fibers, and black for isotropic regions).

References

[1] P. J. Basser, J. Mattiello, D. LeBihan, Estimation of the effective self-diffusion tensor from the NMR spin echo, Journal of Magnetic Resonance, Series B 103 (3) (1994) 247–254. doi:https://doi.org/10.1006/jmrb.1994.1037.

[2] P. J, J. Mattiello, D. LeBihan, MR diffusion tensor spectroscopy and imaging, Biophysical journal 66 (1) (1994) 259–267. doi:10.1016/S0006-3495(94)80775-1.

[3] P. T. Fletcher, Geodesic regression and the theory of least squares on riemannian manifolds, International journal of computer vision 105 (2) (2013) 171–185. doi:https://doi.org/10.1007/s11263-012-0591-y.

[4] P. T. Fletcher, C. Lu, S. Joshi, Statistics of shape via principal geodesic analysis on lie groups, in: 2003 IEEE Computer Society Conference on Computer Vision and Pattern Recognition, 2003. Proceedings., Vol. 1, IEEE, 2003, pp. I–I. doi:10.1109/CVPR.2003.1211342.

[5] K. Krajsek, M. I. Menzel, H. Scharr, A riemannian bayesian framework for estimating diffusion tensor images, International Journal of Computer Vision 120 (3) (2016) 272–299. doi:https://doi.org/10.1007/s11263-016-0909-2.

[6] C. Lenglet, M. Rousson, R. Deriche, O. Faugeras, S. Lehericy, K. Ugurbil, A riemannian approach to diffusion tensor images segmentation, in: Biennial International Conference on Information Processing in Medical Imaging, Springer, 2005, pp. 591–602. doi:https://doi.org/10.1007/11505730_49.

[7] X. Pennec, P. Fillard, N. Ayache, A riemannian framework for tensor computing, International Journal of computer vision 66 (1) (2006) 41–66. doi:https://doi.org/10.1007/s11263-005-3222-z.

[8] K. Oishi, M. M. Mielke, M. Albert, C. G. Lyketsos, S. Mori, Dti analyses and clinical applications in alzheimer's disease, Journal of Alzheimer's Disease 26 (s3) (2011) 287–296. doi:10.3233/JAD-2011-0007.

[9] W. Lee, B. Park, K. Han, Classification of diffusion tensor images for the early detection of alzheimer's disease, Computers in Biology and Medicine 43 (10) (2013) 1313–1320. doi:https://doi.org/10.1016/j.compbiomed.2013.07.004.

[10] M. L. Murphy, T. Frodl, Meta-analysis of diffusion tensor imaging studies shows altered fractional anisotropy occurring in distinct brain areas in association with depression, Biology of mood & anxiety disorders 1 (1) (2011) 1–12. doi:10.1186/2045-5380-1-3.

[11] V. Ressel, H. J. Van Hedel, I. Scheer, R. O. Tuura, Comparison of dti analysis methods for clinical research: influence of pre-processing and tract selection methods, European Radiology Experimental 2 (1) (2018) 1–12. doi:10.1186/s41747-018-0066-1.

[12] W.-S. Tae, B.-J. Ham, S.-B. Pyun, S.-H. Kang, B.-J. Kim, Current clinical applications of diffusion-tensor imaging in neurological disorders, Journal of Clinical Neurology 14 (2) (2018) 129–140. doi:10.3988/jcn.2018.14.2.129.

[13] T. Taoka, M. Morikawa, T. Akashi, T. Miyasaka, H. Nakagawa, K. Kiuchi, T. Kishimoto, K. Kichikawa, Fractional anisotropy–threshold dependence in tract-based diffusion tensor analysis: Evaluation of the uncinate fasciculus in alzheimer disease, American Journal of Neuroradiology 30 (9) (2009) 1700–1703. doi:10.3174/ajnr.A1698.

[14] D. S. Tuch, et al., Diffusion MRI of complex tissue structure, Ph.D. thesis, Massachusetts Institute of Technology (2002). URL http://hdl.handle.net/1721.1/8348

[15] M. Moakher, Fourth-order cartesian tensors: old and new facts, notions and applications, The Quarterly Journal of Mechanics & Applied Mathematics 61 (2) (2008) 181–203. doi:https://doi.org/10.1093/qjmam/hbm027.

[16] E. Özarslan, T. H. Mareci, Generalized diffusion tensor imaging and analytical relationships between diffusion tensor imaging and high angular resolution diffusion imaging, Magnetic Resonance in Medicine: An Official Journal of the International Society for Magnetic Resonance in Medicine 50 (5) (2003) 955–965. doi:10.1002/mrm.10596.

[17] S. Kaushik, J. Kybic, A. Bansal, T. Bihonegn, J. Slovak, Potential biomarkers from positive definite 4th order tensors in hardi, in: 2021 IEEE 18th International Symposium on Biomedical Imaging (ISBI), 2021, pp. 1003–1006. doi:10.1109/ISBI48211.2021.9434144.

[18] E. Özarslan, B. C. Vemuri, T. H. Mareci, Generalized scalar measures for diffusion mri using trace, variance, and entropy, Magnetic Resonance in Medicine: An Official Journal of the International Society for Magnetic Resonance in Medicine 53 (4) (2005) 866–876. doi:10.1002/mrm.20411.

[19] D. S. Tuch, Q-ball imaging, Magnetic Resonance in Medicine: An Official Journal of the International Society for Magnetic Resonance in Medicine 52 (6) (2004) 1358–1372. doi:10.1002/mrm.20279.

[20] E. T. Tan, L. Marinelli, J. I. Sperl, M. I. Menzel, C. J. Hardy, Multi-directional anisotropy from diffusion orientation distribution functions, Journal of Magnetic Resonance Imaging 41 (3) (2015) 841–850. doi:https://doi.org/10.1002/jmri.24589.

[21] L. J. Volz, M. Cieslak, S. Grafton, A probabilistic atlas of fiber crossings for variability reduction of anisotropy measures, Brain Structure and Function 223 (2) (2018) 635–651. doi:10.1007/s00429-017-1508-x.

[22] A. Ghosh, T. Papadopoulo, R. Deriche, Biomarkers for HARDI: 2nd & 4th order tensor invariants, in: 2012 9th IEEE International Symposium on Biomedical Imaging (ISBI), IEEE, 2012, pp. 26–29. doi:10.1109/ISBI.2012.6235475.

[23] L. Astola, L. Florack, Finsler geometry on higher order tensor fields and applications to high angular resolution diffusion imaging, International Journal of Computer Vision 92 (3) (2011) 325–336. doi:https://doi.org/10.1007/978-3-642-02256-2_19.

[24] L. Astola, A. Jalba, E. Balmashnova, L. Florack, Finsler streamline tracking with single tensor orientation distribution function for high angular resolution diffusion imaging, Journal of Mathematical Imaging and Vision 41 (3) (2011) 170–181. doi:https://doi.org/10.1007/s10851-011-0264-4.

[25] N. Sepasian, J. H. ten Thije Boonkkamp, L. M. Florack, B. M. T. H. Romeny, A. Vilanova, Riemann-finsler multi-valued geodesic tractography for hardi, in: Visualization and Processing of Tensors and Higher Order Descriptors for Multi-Valued Data, Springer, 2014, pp. 209–225. doi:https://doi.org/10.1007/978-3-642-54301-2_9.

[26] A. Barmpoutis, M. S. Hwang, D. Howland, J. R. Forder, B. C. Vemuri, Regularized positive-definite fourth order tensor field estimation from dw-mri, NeuroImage 45 (1) (2009) S153–S162. doi:10.1016/j.neuroimage.2008.10.056.

[27] A. Barmpoutis, B. C. Vemuri, A unified framework for estimating diffusion tensors of any order with symmetric positive-definite constraints, in: 2010 IEEE international symposium on biomedical imaging: from nano to macro, IEEE, 2010, pp. 1385–1388. doi:10.1109/ISBI.2010.5490256.

[28] C. Beaulieu, The basis of anisotropic water diffusion in the nervous system – a technical review, NMR in Biomedicine 15 (7-8) (2002) 435–455. arXiv:https://analyticalsciencejournals.onlinelibrary.wiley.com/doi/pdf/10.1002/nbm.782, doi:https://doi.org/10.1002/nbm.782.

[29] A. Ghosh, T. Papadopoulo, R. Deriche, Generalized invariants of a 4th order tensor: Building blocks for new biomarkers in dMRI, in: Proceedings of the Computation Diffusion MRI Workshop at the MICCAI Conference, 2012, p. 165–173.

[30] S. Kaushik, J. Slovak, HARDI segmentation via fourth order tensors and anisotropy preserving similarity measures, Journal of Mathematical Imaging and Vision 2018 (5) (2019) 12. doi:https://doi.org/10.1007/s10851-019-00897-w.

[31] P. J. Basser, S. Pajevic, Spectral decomposition of a 4th-order covariance tensor: Applications to diffusion tensor MRI, Signal Processing 87 (2) (2007) 220–236. doi:https://doi.org/10.1016/j.sigpro.2006.02.050.

[32] R. M. Brannon, Rotation, Reflection, and Frame Changes, 2053-2563, IOP Publishing, 2018. doi:10.1088/978-0-7503-1454-1.